Neural Computing and Applications
https://doi.org/10.1007/s00521-021-06336-5

S.I.: HUMAN-IN-THE-LOOP MACHINE LEARNING AND ITS APPLICATIONS

Joint regularization and low-rank fusion for atmospheric turbulence removal

Yanyun Qu[1] · Wenjin Yang[1] · Yuan Xie[2] · Weiwei Wu[3] · Yang Wu[4] · Hanzi Wang[1]

Received: 23 November 2020 / Accepted: 18 July 2021

Abstract
Atmospheric turbulence removal remains a challenging task, because it is very difficult to mitigate geometric distortion and remove spatially and temporally variant blur. This paper presents a novel strategy for atmospheric turbulence removal by characterizing local smoothness, nonlocal similarity and low-rank property of natural images. The main contributions are three folds. First, a joint regularization model is made which combines nonlocal total variation regularization and steering kernel regression total variation regularization in order that reference image enhancement and image registration are jointly implemented on geometric distortion reduction. Secondly, a fast split Bregman iteration algorithm is designed to address the joint variation optimization problem. Finally, a weighted nuclear norm is introduced to constrain the low-rank optimization problem to reduce blur variation and generate a fusion image. Extensive experimental results show that our method can effectively mitigate geometric deformation as well as blur variations and that it outperforms several other state-of-the-art turbulence removal methods.

Keywords Atmospheric turbulence · Joint regularization · Low-rank · Weight nuclear norm minimization

1 Introduction

Atmospheric turbulence can strongly affect the long-distance imaging system, and it results in image degeneration with geometric distortion, blur, and noises, because the refractive index is changed randomly along the optical transmission path affected by atmospheric turblulence. Turbulence degrades the imaging quality and makes the subsequent image analysis difficult, e.g., it may result in the failure of an automatic target recognition system, because an object appearance model may be very different from the pretrained system. A core problem caused by atmospheric turbulence is that the geometric distortion and space-time-varying blur are jointly imposed on an long-distance imaging system. As we know, image restoration is still a difficult task until now [1–5], and it is very challenging to correct the geometric distortion and reduce the spacially and temporally variant blur simultaneously. Supposing that the scene and the image sensor are both static, the degradation of an image caused by atmospheric turbulence is modeled as follows [6],

$$f_i(u(\mathbf{x})) = D_{i,\mathbf{x}}(H(u(\mathbf{x}))) + \varepsilon_i \quad \forall i, i \in [1, 2, \ldots, N] \tag{1}$$

✉ Yanyun Qu
yyqu@xmu.edu.cn

Wenjin Yang
wjyang6@stu.xmu.edu.cn

Yuan Xie
yxie@cs.ecnu.edu.cn

Weiwei Wu
www619471234@gmail.com

Yang Wu
dylanywu@tencent.com

Hanzi Wang
hanzi.wang@xmu.edu.cn

[1] Department of Computer Science and Technology, School of Informatics, Xiamen University, Xiamen, China

[2] School of Computer Science and Technology, East China Normal University, Shanghai, China

[3] Beijing Kwai Technology Co., Ltd., Beijing, China

[4] Applied Research Center (ARC), Tencent PCG, Shenzhen, China

Published online: 06 August 2021

where u denotes the original static scene, f_i represents the ith observed frame, N is the number of observed frames, $\mathbf{x} = (x, y)^T$, is the position of a pixel, and ε_i is the noise. In Eq. (1), H represents a diffraction-limit point spread function (PSF) which is spacial invariant, and it can be treated as a blurring kernel due to an optic sensor. $D_{i,\mathbf{x}}$ is a turbulence-caused PSF, which is defined as a function in spatial-temporal space.

Great progresses are made in atmospheric turbulence removal. The reviews about atmospheric turbulence removal were given in [7, 8]. Many researchers treated the turbulence removal as a deconvolution problem. Li et al. [9] used principal component analysis to explicitly model the multichannel image deconvolution problem for restoring atmospheric turbulence images. Harmeling et al. [10] proposed an online deconvolution method for atmospheric turbulence removal, while Tahtali et al. [11] focused on deconvolution based on filtering methods. Mao and Gilles [12] made a TV-based optimal model for deconvolution which was solved by Bregman algorithm. However, the deconvolution methods cannot correct the geometric distortion very well.

Different from the deconvolution methods, some researches were made to mitigate the turbulence effect through removing geometric distortion and deblurring. There exit two main categories: the multi-frame reconstruction approaches and the lucky imaging approaches. In the multi-frame reconstruction approaches [13, 14], each observed frame is registered to a reference image with respect to a fixed reference grid by a nonrigid image registration method. The registration parameters of each frame are used to estimate the corresponding motion field. After that, a Bayesian method is employed to generate a sharp image. The limitation of [13, 14] is that the PSF is approximated by a fixed Gaussian model rather than the spatially and temporally variant PSF. Different from [13, 14] which processed an image as a whole during registration, efficient filter flow (EFF) [15] first divided each frame into overlapping patches. Considering that these patches were small in size, the patches were supposed to contain space-invariant blur, and thus they were regarded as isoplanatic regions. Then a PSF was estimated separately for each patch by the multi-frame blind deconvolution. The final output was generated by a non-blind deconvolution algorithm. This method actually suppressed the turbulence effect, but it neglected the removal of diffraction-limited blur due to absence of the prior knowledge. Moreover, the final results contained strong blurring artifacts because the local PSF was not estimated accurately.

Lucky imaging assumption is popularly used in turbulence removal methods. Some methods [16–19] selected lucky frames and fused them to reduce the blurring effects. These methods assumed that the observation image is under short exposure and some sufficiently sharp images can be made randomly. The assumption is desired in many astronomical image processing. Voronatsov and Carhart [17] first detected lucky region which is a local sharpness region and is assumed to be affected only by a diffraction-limited PSF and then fused the sharpest regions to generate a large deblurred image. Similar to [17], Joshi et al. [20] first utilized alignment operation to correct the local geometric deformation. Then they implemented weight combination on the lucky regions to form a sharp image. Aubailly et al. [21] selected lucky regions by image quality mapping and then fused the selected regions into the video stream. However, lucky imaging method requires to divide an image into some image regions. For this reason, its performance on image restoration is very limited.

Recently, Zhu and Milanfar [6] proposed a unified framework which not only removed geometric distortion but also reduced the space-time-varying blur. In [6], a symmetric constraint-based B-spline registration was proposed in order to overcome the geometric distortion, and then a kernel regression reconstruction method was utilized in order to generate the near-diffraction-limited image. At last, the blind deconvolution method was adopted to deblur the near-diffraction-limited image.

Our previous work [22] improved Zhu's method by making a hybrid total variation model for geometric correction and by implementing deformation-guided kernel regression for near-diffraction-limited image reconstruction. However, the used image priors are limited and the deformation-guided kernel regression has high computational complexity. It is known that the image prior knowledge has an important effect on the image restoration performance. Thus, it is the core of turbulence removal to design effective regularization terms. Our previous work [22] used the classic regularization terms such as the nonlocal total variation (NLTV) and local total variation. Though the regularization terms are effective in edge preserving and smooth regions restoration, they often smear out the image details. In this paper, we use more effective image priors such as steering kernel regression total variation (SKRTV) and the low-rank property of natural images. SKRTV is better to preserve edges along their directions than the common local total variation. Moreover, the deformation-guided kernel regression in our previous work [22] is very time-consuming in the stage of the near-diffraction-limited image reconstruction because SVD is implemented for each pixel. In this paper, we implement weight nuclear norm maximization (WNNM) algorithm [23] which is an improved low-rank decomposition method for diffraction-limited image reconstruction. And it has been recognized that WNNM can achieve better

denoising and deblur performance than the regression-based methods.

The contributions of this paper are three folds: (1) A joint regularization model with NLTV and SKRTV is proposed for geometric deformation removal. (2) The SBI algorithm is developed for solving the joint TV-based regularization model. (3) The WNNM algorithm is utilized to reduce the blur variation for obtaining a near-diffraction-limited image.

Our paper is organized as follows. The framework of our method is described in Sect. 2. Then, deformation removal through variation model is detailed in Sect. 3. In Sect. 4, the reconstruction of a near-diffraction-limit image by capturing the low-rank priori is introduced. Section 5 shows experimental results. Section 6 concludes this paper and discusses future work.

2 Turbulence removal scheme overview

We adopt Zhu's framework [6] whose core idea is to transform a space-time-varying blur to a shift invariant blur. The framework is shown in Fig. 1. There are four key steps: initial reference image construction, image registration, space-time-varying blur reduction, and deconvolution. Considering the low-rank priori of the video frames, the frames are regarded as the "dancing images" of the latent scene. We employ robust principal component analysis (RPCA) [24] to generate the original reference image. After that, we iteratively enhance the reference image and register image frames to the reference image based on a joint regularization model. Furthermore, we develop an algorithm based on WNNM to reduce time-varying blur for a near-diffraction-limited image reconstruction, which is first done for video denoising. Different from Zhu's method, we focus on two aspects: (1) alternatively optimizing nonrigid registration and the enhancement of the reference image in order to improve the quality of geometric correction, (2) implementing WNNM for near-diffraction-limited image reconstruction.

3 Iterative nonrigid image registration

In the first step, our approach first registers each frame onto a reference image, given an observed video. There are two important factors that affect the registration results: how to generate the reference image and how to register a frame to the reference image. We focus on improving both the quality of reference image and image registration in this paper. To this end, an algorithm which iteratively enhances the reference image and mitigates the geometric deformation has been developed.

We first discuss how to produce the reference image. By assuming that both the camera and the scene are static and that the motion is only due to the air turbulence, the observed frames take on "image dancing" phenomena. Inspired by the low-rank priori [25], the low-rank part of the sequence can be considered an intrinsic component of "image dancing"; therefore, we further regard each image as a combination of the stable low-rank part and the sparse part (such as noises and distortion), and we solve the optimization problem as Eq. (2),

$$\begin{aligned} &\text{minimize} \|R\|_* + \lambda \|S\|_1 \\ &s.t.\ R + S = G \end{aligned} \tag{2}$$

where G is the matrix and its columns are generated by stretching a frame f_i to a vector, R is the low-rank part of the matrix G, and S is the sparse matrix. $\|\cdot\|_*$ denotes the nuclear norm which is defined as the sum of all singular values, and $\|\cdot\|_1$ is the ℓ_1 norm. We exploit RPCA [24] to

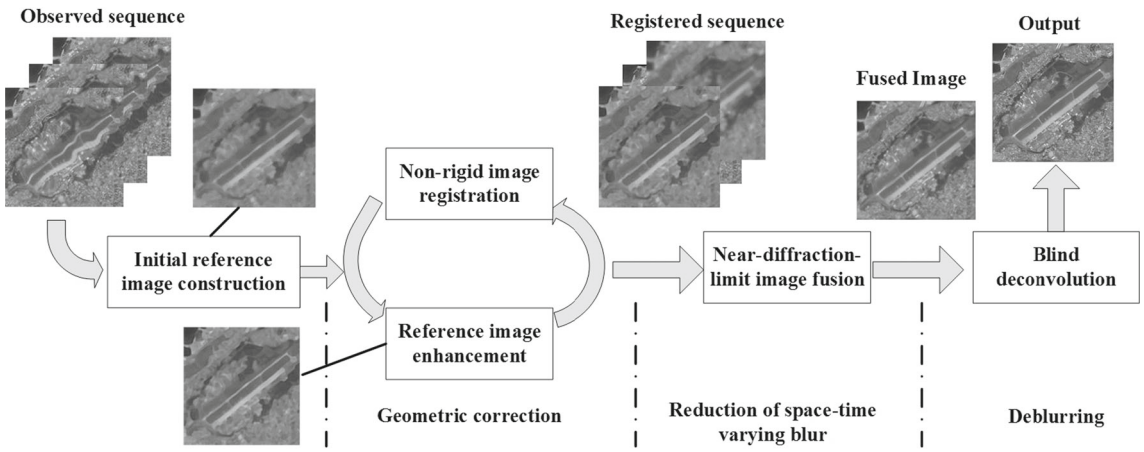

Fig. 1 The framework of our approach. There are four important steps: initial reference image construction, image registration, near-diffraction limit image fusion, and image deconvolution

estimate the matrix R. After that, we compute the column average of the matrix R, which is regarded as the concatenated column of the initial reference image.

3.1 Reference image enhancing via a joint regularization model

In this section, we assume that each observed frame is generated from the reference image u with a warping transformation, and Eq. (1) is reformulated as,

$$f_i(u) = D_{i,\mathbf{x}}u + \varepsilon_i \quad \forall i, i \in [1, 2, \ldots, N] \tag{3}$$

Due to deformation and noise, the deformation removal is a typical ill-posed problem. Hence, we incorporate two effective regularizers to make the problem well-posed, namely NLTV and SKRTV. NLTV is used for preserving the nonlocal self-similarity, and SKRTV is used for keeping the local data-driven smoothness. Thus, we make the model as follows:

$$\min_u \frac{1}{N}\sum_i \|\Phi_i u - f_i\|_2^2 + \mu_1 \varphi_{nl}(u) + \mu_2 \varphi_l(u) \tag{4}$$

The first term of Eq. (4) is to estimate the fidelity of the observed frames $\{f_i\}_{i=1}^N$ to the transformations of the reference image, and Φ_i is a transformation operator which can map the reference image to the observed frame. In this paper, the B-spline registration method [26, 27] is used to compute the operator Φ_i. The last two terms are the NLTV regularization and SKRTV regularization term, respectively. In the following, we briefly introduce the two regularization terms.

NLTV is effective for image restoration which is employed to regularize the ill-posed deformation removal problem. Under the assumption of nonlocal self-similarity, the similar patches searched in different locations can be regarded as the multiple observations of the target patch. The NLTV regularization term is formulated as,

$$\varphi_{nl}(u) = |\nabla_N u| = \sum_i \sum_{j \in P(\mathbf{x}_i)} |u(\mathbf{x}_j) - u(\mathbf{x}_i)| \sqrt{w_N(i,j)} \tag{5}$$

where $w_N(i,j)$ is the similarity weight which measures the similarity between the image patch centered at the pixel position $\mathbf{x}_i$ and the image patch centered at the pixel position $\mathbf{x}_j$, and $P(\mathbf{x}_i)$ denote the index set which contains the indexes of image patches similar to the image patch at the position $\mathbf{x}_i$. We define the extraction operator as $\mathcal{R}_{\mathbf{x}_i}u$ which represents the patch centered at $\mathbf{x}_i$. The patch size is $L_{nl} \times L_{nl}$. We search the similar patch in a $W \times W$ window centered at x_i. The most similar N patches are kept. The similarity weight between the patches at position $\mathbf{x}_i$ and $\mathbf{x}_j$ is defined as,

$$w_N(i,j) = \exp\left(-\frac{\|\mathcal{R}_{\mathbf{x}_i}u - \mathcal{R}_{\mathbf{x}_j}u\|^2}{{h_n}^2}\right) \tag{6}$$

where h_n denotes the global parameter controlling the speed of degradation of exponential function.

As for the third term of Eq. (4), it is the SKRTV regularization term. It has been proved that SKR [28] is effective for image restoration. And SKR is a local approximate method, which approximates a point by Taylor expansion. And it can be modeled as a weighted least square method,

$$\beta_i = \underset{\beta_i}{\operatorname{argmin}} \sum_i \|y - \Psi\beta_i\|_{K_{h_k}}^2 \tag{7}$$

where y is the column vector and its elements are the intensities of the pixels which are the neighbors of the pixel $\mathbf{x}_i$. h_k is a smoothing parameter and $K_{h_k}(\mathbf{x_i} - \mathbf{x}) = \frac{\sqrt{\det(C_i)}}{2\pi {h_k}^2}\exp(-\frac{(\mathbf{x}_i - \mathbf{x})^{\mathrm{T}} C_i (\mathbf{x_i} - \mathbf{x})}{2{h_k}^2})$ is the weight function where the matrix C_i represents the symmetric gradient covariance derived from $\mathbf{x}_i$ in the horizontal and vertical direction. Ψ is the polynomial basis, defined by

$$\Psi = \begin{bmatrix} 1 & (\mathbf{x}_i - \mathbf{x}_{i1})^{\mathrm{T}} & \mathrm{vech}^{\mathrm{T}}(\mathbf{x}_i - \mathbf{x}_{i1})(\mathbf{x}_i - \mathbf{x}_{i1})^{\mathrm{T}} \\ 1 & (\mathbf{x}_i - \mathbf{x}_{i2})^{\mathrm{T}} & \mathrm{vech}^{\mathrm{T}}(\mathbf{x}_i - \mathbf{x}_{i2})(\mathbf{x}_i - \mathbf{x}_{i2})^{\mathrm{T}} \\ \vdots & \vdots & \vdots \\ 1 & (\mathbf{x}_i - \mathbf{x}_{il})^{\mathrm{T}} & \mathrm{vech}^{\mathrm{T}}(\mathbf{x}_i - \mathbf{x}_{il})(\mathbf{x}_i - \mathbf{x}_{il})^{\mathrm{T}} \end{bmatrix} \tag{8}$$

where $\mathrm{vech}^{\mathrm{T}}\{\begin{bmatrix} a & b \\ b & c \end{bmatrix}\} = [a \quad b \quad c]$, and $\mathbf{x}_{is}, (s = 1, 2, \cdots, l)$ is the neighbor of the pixel $\mathbf{x}_i$.

The solution of Eq. (7) is

$$\hat{\beta}_i = \left(\Psi^{\mathrm{T}} K \Psi\right)^{-1} \Psi^{\mathrm{T}} K y \tag{9}$$

where

$$K = \mathrm{diag}\{K_{h_k}(\mathbf{x_1} - \mathbf{x}), K_{h_k}(\mathbf{x_2} - \mathbf{x}), \ldots, K_{h_k}(\mathbf{x_l} - \mathbf{x})\}$$

is a diagonal matrix. The pixel value at $\mathbf{x}_i$ can be estimated as $R(\mathbf{x}_i) = e_1^{\mathrm{T}}\hat{\beta}_i$ where $e_1 = [1 \ 0 \ \cdots \ 0]^{\mathrm{T}}$ is the first column of identity matrix. The weights between the position $\mathbf{x}_i$ and its neighbors are formulated as $[w_s(i,i1) \ w_s(i,i2) \ \cdots \ w_s(i,il)] = e_1^{\mathrm{T}}(\Psi^{\mathrm{T}}K\Psi)^{-1}\Psi^{\mathrm{T}}K$.

Thus, SKRTV regularization terms can be formulated as,

$$\varphi_l(u) = |\nabla_S u| = \sum_i \sum_{j \in \aleph(\mathbf{x}_i)} |u(\mathbf{x}_j) - u(\mathbf{x}_i)| \sqrt{w_s(i,j)} \tag{10}$$

where $\aleph(\mathbf{x}_i)$ is the neighbor of the position $\mathbf{x}_i$, and $w_s(i,j)$ is the weight generated by SKR. Note that $\nabla_N u$ and $\nabla_S u$ are vectors which contain all nonlocal gradients generated by an image.

We plug Eqs. (5) and (10) into Eq. (4) and obtain the optimization problem as,

$$\min_u \underbrace{\frac{1}{N}\sum_i \|\Phi_i u - f_i\|_2^2}_{E(u)} + \underbrace{\mu_1 \overbrace{|\nabla_N u|}^{J_N(u)} + \mu_2 \overbrace{|\nabla_S u|}^{J_S(u)}}_{J(u)} \tag{11}$$

where μ_1 and μ_2 are the two trade-off parameters which balance the fidelity term, the NLTV regularization term, and the SKRTV regularization term.

3.2 Fast Bregman algorithm

Equation (11) is a classic TV-based problem, and it is solved by SBI [29] in our paper. SBI is a typical method for a class of l_1 norm-related minimization problems. The core of SBI is to transform an unconstraint optimization problem into a constraint optimization problem. And it has been proved that SBI converges fast for the TV-based optimization problem.

Let us consider a general optimization problem,

$$\min_u |J(u)| + E(u),$$

where $E(u)$ is differentiable. And it can be converted a constrained optimization problem,

$$\min_u |d| + E(u) \quad s.t. \quad d = J(u) \tag{12}$$

SBI is shown in Algorithm 1.

Algorithm 1 Split Bregman Iteration (SBI)

1: Set $k = 0$, initiate $\lambda > 0$, $u^0 = 0$, $b^0 = 0$, $d^0 = 0$,
2: **repeat**
3: $u^{k+1} = \min_u E(u) + \frac{\lambda}{2}\|d^k - J(u) - b^k\|_2^2$;
4: $d^{k+1} = \min_u |d| + \frac{\lambda}{2}\|d - J(u^{k+1}) - b^k\|_2^2$;
5: $b^{k+1} = b^k + (J(u^{k+1}) - d^{k+1})$;
6: $k \leftarrow k + 1$;
7: **until** stopping rule is satisfied

Due to the decoupling operation separating u from l_1 norm problem, the optimization problem for u^{k+1} in Line 3 is now differentiable. A variety of optimization methods can be adopted to solve this problem. For the solution of the optimization problem in Line 4 which is coupled with the l_1 portion of the minimization problem, shrinkage operators are used to compute the optimal value of d,

$$d_j^{k+1} = shrink\left(J(u)_j + b_j^k, \frac{1}{\lambda}\right) \tag{13}$$

where $shrink(x, \gamma) = \frac{x}{|x|} * \max(|x| - \gamma, 0)$.

We first convert Eq. (11) to the optimization problem with constraints as follows,

$$\hat{u} = \min_u \frac{1}{2N}\sum_i \|\Phi_i u - f_i\|_2^2 + \mu_1|d_N| + \mu_2|d_S| \quad s.t. \quad d_N = \nabla_N u, \quad d_S = \nabla_S u \tag{14}$$

First, we define $E(u) = \frac{1}{2N}\sum_i \|\Phi_i u - f_i\|_2^2$, $d = \begin{bmatrix}\mu_1 d_N \\ \mu_2 d_S\end{bmatrix}$, $J(u) = \begin{bmatrix}\mu_1 \nabla_N u \\ \mu_2 \nabla_S u\end{bmatrix}$.

According to SBI, Line 3 in Algorithm 1 becomes:

$$\begin{aligned} u^{k+1} &= \underset{u}{\text{argmin}} E(u) + \frac{\lambda}{2}\left\|d^k - J(u) - b^k\right\|_2^2 \\ &= \text{argmin}_u \frac{1}{2N}\sum_i \|\Phi_i u - f_i\|_2^2 \\ &\quad + \frac{\lambda\mu_1^2}{2}\left\|d_N^k - \nabla_N u - b_N^k\right\|_2^2 + \frac{\lambda\mu_2^2}{2}\left\|d_S^k - \nabla_S u - b_S^k\right\|_2^2 \end{aligned} \tag{15}$$

where $b^k = \begin{bmatrix}\mu_1 b_N^k \\ \mu_2 b_S^k\end{bmatrix}$.

Next, Line 4 in Algorithm 1 becomes:

$$\begin{aligned} d^{k+1} &= \underset{d}{\text{argmin}}|d| + \frac{\lambda}{2}\left\|d - J\left(u^{k+1}\right) - b^k\right\|^2 \\ &= \text{argmin}_d \mu_1|d_N| + \mu_2|d_S| \\ &\quad + \frac{\lambda}{2}\left\|\begin{bmatrix}\mu_1 d_N \\ \mu_2 d_S\end{bmatrix} - \begin{bmatrix}\mu_1 \nabla_N u^{k+1} \\ \mu_2 \nabla_S u^{k+1}\end{bmatrix} - \begin{bmatrix}\mu_1 b_N^k \\ \mu_2 b_S^k\end{bmatrix}\right\|_2^2 \end{aligned} \tag{16}$$

Obviously, the optimization problem Eq. (16) can be decoupled and thus can be solved separately, resulting in

$$d_N^{k+1} = \underset{d_N}{\text{argmin}}\left\{|d_N| + \frac{\lambda\mu_1}{2}\left\|d_N - \nabla_N u^{k+1} - b_N^k\right\|^2\right\} \tag{17}$$

$$d_S^{k+1} = \underset{d_S}{\text{argmin}}\left\{|d_S| + \frac{\lambda\mu_2}{2}\left\|d_S - \nabla_S u^{k+1} - b_S^k\right\|^2\right\} \tag{18}$$

Line 5 in Algorithm 1 becomes:

$$\begin{bmatrix}\mu_1 b_N^{k+1} \\ \mu_2 b_S^{k+1}\end{bmatrix} = \begin{bmatrix}\mu_1 b_N^k \\ \mu_2 b_S^k\end{bmatrix} + \left(\begin{bmatrix}\mu_1 \nabla_N u^{k+1} \\ \mu_2 \nabla_S u^{k+1}\end{bmatrix} - \begin{bmatrix}\mu_1 d_N^{k+1} \\ \mu_2 d_S^{k+1}\end{bmatrix}\right) \tag{19}$$

which can be simplified into the following two expressions:

$$b_N^{k+1} = b_N^k + \nabla_N u^{k+1} - d_N^{k+1} \tag{20}$$

$$b_S^{k+1} = b_S^k + \nabla_S u^{k+1} - d_S^{k+1} \tag{21}$$

Equation (15) can be solved as,

$$(1-\lambda_N\lambda\Delta_N-\lambda_S\lambda\Delta_S)u^{k+1} = \frac{1}{N}\sum_i \Phi_i^{-1}f_i+\lambda_N\lambda div_N(b_N^k-d_N^k)+\lambda_S\lambda div_S(b_S^k-d_S^k) \tag{22}$$

where $\lambda_N=\mu_1^2$ and $\lambda_S=\mu_2^2$. In Eq. (22), $div_N()$ and $div_S()$ are the divergence operators. Δ_N and Δ_S are the Laplacian operators, which are the nonlocal operators detailed in [30], similar to the common divergence operator and Laplacian operator. Equation (22) is a typical system of linear algebraic equations and can be solved by Gauss-Seidel algorithm. And the optimization problems Eqs. (18) and (17) can be obtained by applying the shrinkage operator,

$$d_N^{k+1}=shrinkage\left(\nabla_N u^{k+1}+b_N^k,\frac{1}{\lambda\mu_1}\right) \tag{23}$$

$$d_S^{k+1}=shrinkage\left(\nabla_S u^{k+1}+b_S^k,\frac{1}{\lambda\mu_2}\right) \tag{24}$$

After the convergence of the optimization problem (14), the observed frames $\{f_i\}_{i=1}^N$ are registered onto the enhanced reference image, and then the registered frame sequence $\{\tilde{f}_i\}_{i=1}^N$ is achieved. The proposed SBI algorithm for joint reference image enhancement and image registration is described in Algorithm 2. Firstly, the weights for NLTV and SKRTV are computed. And then, the algorithm enters a loop of image registration and updating. In the step of image registration, each frame is registered onto the initial reference image. After that, the reference image is updated according to SBI. The loop stops until the accuracy of image registration satisfies the setting threshold.

Algorithm 2 SBI for the joint regularization model

Input: an observed video $\{f_i\}_{i=1}^N$
Output: Clean image u and the registered image $\{\tilde{f}_i\}_{i=1}^N$
Initialize the reference image u by RPCA
Compute the NLTV weights
Compute the SKRTV weights
Set $\lambda>0$, $\mu_1>0$, $\mu_2>0$, $t=0$, $d_N^t=b_N^t=d_S^t=b_S^t=0$,
for each frame f_k **do**
    Initialize $\tilde{f}_k=f_k$
    Register each frame $\tilde{f}_k$ onto the reference image $u^t=u$, obtain the transform matrix Φ_k
end for
while $\frac{1}{N}\sum_i\|\Phi_i u-f_i\|>\varepsilon$ **do**
    while Objective (14) is decreasing **do**
        Update u^{t+1} by (22)
        Update d_N^{t+1} by (23)
        Update d_S^{t+1} by (24)
        Update b_N^{t+1} by (20)
        Update b_S^{t+1} by (21)
        $t=t+1$
    end while
    $\tilde{f}_i=\tilde{f}_i+f_i-\Phi_i u^t$
    $u=u^t$
    Register each frame $\tilde{f}_i$ onto the reference image u, update the transform matrix Φ_k
end while

4 Near-diffraction-limited image reconstruction via WNNM

For the registered video frames $\{\tilde{f}_i\}_{i=1}^N$, the turbulence caused PSF can be regarded to be patch-wise constant and time varying according to [6]. Thus, we reduce the blur variation to restore a diffraction-limited image. After that, a global deconvolution method can be used for deburring. Noises are one of the causes resulting in blur variation as discussed in [6], which may lead to artifacts during deconvolution, so noises need to be suppressed. It is proved that WNNM is very effective for image denoising [23]. Thus, the WNNM algorithm is developed for reducing blur variation[31].

Each registered frame $\tilde{f}_i$ is viewed as a combination of the diffraction-limited image and the noise. Our purpose here is to denoise the registered frames. We exploit the temporal redundancy in the registered frames to remove the image noises, as shown in Fig. 2. The patches at the same position of each registered frame, such as the green boxes, can be regarded to be from a latent state, such as the red

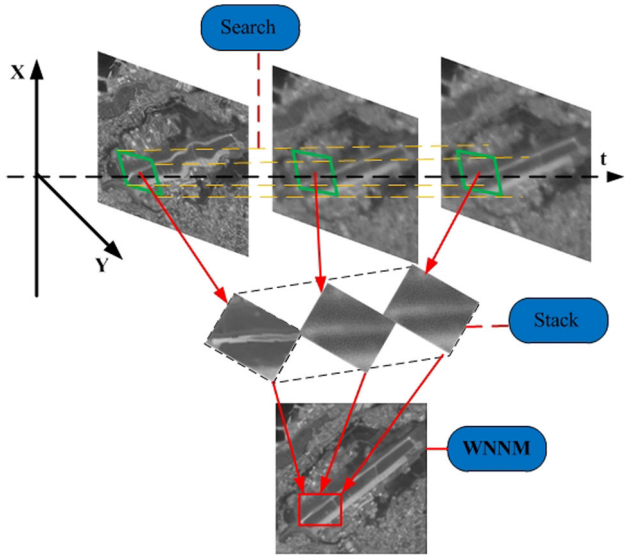

Fig. 2 Illustration of the near-diffraction limit image fusion based on WNNM

box. And the latent state is solved by WNNM. Let's define the noisy frame as $\{X_i\}_{i=1}^{N}$. The reference image is denoted as X_0. For an image patch $\mathcal{R}_{\mathbf{x_i}}X_0$ centered at the position $\mathbf{x}_i$ in the reference image X_0, its similar patches are extracted from other frames with the same position. Given that all similar image patches $\{\mathcal{R}_{\mathbf{x_i}}X_k\}_{k=0}^{N}$ are found, each patch is stretched into a column vector. All the column vectors construct the matrix R_i which is formulated as follows,

$$R_i = Q_i + N_i \tag{25}$$

where Q_i is the low-rank part of the matrix R_i, and N_i is the noise matrix. Now, we convert the denoising problem to a low-rank approximation problem,

$$\min_{Q_i} \|R_i - Q_i\|_F^2 + \|Q_i\|_{W,*}^2 \tag{26}$$

where $\|Q_i\|_{W,*} = \sum_j w_j\sigma_j(Q_i)$ is the weighted nuclear norm, $W = [w_1, w_2, \cdots, w_K]$, $(W_j \geq 0)$ is a nonnegative weight vector and $\sigma_j(Q_i)$ is the jth singular value of the matrix Q_i. According to Theorem 2 in [23], the global optimal solution of Eq. 26 is obtained,

$$\tilde{Q}_i = US_W(\Sigma)V^T \tag{27}$$

where $R_i = U\Sigma V^{\mathrm{T}}$ is the SVD of R_i and $S_W(\Sigma)$ is a soft-thresholding operator with weight vector W,

$$S_W(\Sigma) = \max_j(\Sigma_{ii} - w_i, 0) \tag{28}$$

Because the larger singular values of R_i are more important than the smaller singular values, the larger singular values should have smaller shrinkage than the smaller singular values. Furthermore, it is proved that WNNM can converge to a fixed point if the weights are distributed in a non-ascending order, $0 \leq w_1 \leq w_2 \leq \ldots \leq w_K$ [23]. Thus, the weights are adopted to be the inversely proportional to the singular values of R_i, that is,

$$w_i = \frac{c\sqrt{N}}{\sigma_i(R_i) + \varepsilon} \tag{29}$$

where N is the number of frames and $\varepsilon = 10^{-16}$ is to avoid dividing by 0. We process each image patch of the reference image by using sliding window scheme and fuse the frames by averaging the denoising frames. We summarize the image fusion based on WNNM in Algorithm 3.

After image fusion, we obtain the near-diffraction-limit image which can be treated as the blurry result of a latent scene state. We assume that the degradation model is $\hat{X} = H(u) + \varepsilon$, where ε is the error generated by the process of solving $\hat{X}$. We adopt the blind deconvolution model to solving the latent variant. The details are shown in [32]. Now, we summarize the complete procedure of turbulence removal in Algorithm 4.

Algorithm 3 Image fusion by WNNM

Input: Noisy video $\{\tilde{f}\}_{i=1}^{N}$ obtained after image registration

Output: Clean image $\hat{X}$, the output is the fusion image which is the average of $\{\hat{X}_i^{(K)}\}_{i=0}^{N}$

Initialize $\hat{X}_0^{(0)} = X_0$, $\tilde{f}_0^{(0)} = X_0$, $\hat{X}_i^{(0)} = \tilde{f}_i (i = 1, 2, \cdots, N)$ % X_0 is the reference image
for $k = 1$ to K **do**
  for $i = 0$ to N **do**
    Iterative regularization $\tilde{f}_i^{(k)} = \hat{X}_i^{(k-1)} + \delta(\tilde{f}_i - \tilde{f}_i^{(k-1)})$
  end for
  for each patch centered at each sampling point x_i **do**
    Construct the matrix R_i
    Singular value decomposition $[U, \Sigma, V] = \mathrm{SVD}(R_i)$
    Estimate weight vector w using Eq. (29)
    Obtain the estimation $Q_i = US_W(\Sigma)V^{\mathrm{T}}$
  end for
  Aggregate Q_i to form the clean image $\hat{X}_i^{(k)}$.
end for

Algorithm 4 Turbulence Removal Algorithm

Input: Observed video frames $\{f_i\}_{i=1}^{N}$
Output: Restored image u

while $iter \leq iter_{max}$ **do**
  Stretch each frame into a vector, and stack the vectors into a matrix V
  $u \leftarrow$ Low-rank-decomposition(V)
  Compute the registered frames $\{\tilde{f}_i\}_{i=0}^{N}$ and the enhanced reference image u via Algorithm 2
end while
Reconstruct the near diffraction-limited image $\hat{X}$ via Algorithm 3
Restore the image $\hat{X}$ from blurring for a latent clear image u

5 Experimental results and analysis

5.1 Experiment setup

Extensive experiments have been conducted to evaluate our approach on nine image sequences including some representative videos used in Zhu's work [6]. The thumbnail images from the videos are shown in Fig. 3. The testing sequences, *Airport*, *Arch*, *City_strong*, *City_weak*, *Base_strong*, *Base_weak* are simulated videos, and *Building*, *Chimney*, and *Wall* are real videos. For the evaluation of our method, we use the simulation method detailed in [6] and generate degraded videos by simulating different degrees of turbulence. The simulation algorithm has three critical factors: a spatially invariant diffraction-limited PSF, spatially variant PSFs, and the deformation field. A set of control points affects the deformation field, and they are offset randomly according to the Gaussian distribution with the mean of zero and the variance of σ_d^2. For the spacial variant blur, a video is convolved by a set of PSFs which are Gaussian functions with variances depending linearly to the counterpart local motion energy whose computation is detailed in [6]. In our experiments, the interval of control points is d_g and the number of PSFs is set to the number of the control points. A fast blur algorithm [33], combining the overlapped convolution schemes [34] with the linear interpolation of measured PSFs, is used to generate the spatially-variant blur. Two groups of parameters, which are shown in Table 1, are applied on the two videos of *City* and *Base*, respectively, leading to four simulated videos: *City_strong*, *City_weak*, *Base_strong*, and *Base_weak*. And the other simulated videos are generated by the weak turbulence.

All the parameter settings used in our experiments are summarized in Table 2. In our method, we utilize the deconvolution code [32] provided by the authors in the last step and we implement two sets of parameters on the real and simulated data, respectively. Three parameters of deconvolution code [32] are tunable: the blur kernel size, the noise level, and the weight for completeness of debluring, while setting all other parameters as the default values. And the settings are detailed in [32]. In the simulated experiments, the tunable parameters are set to (5, 5, 0.03, 0.2), where the first two parameters denote the blur kernel size is 5×5. The tunable parameters are set to (9, 9, 0.05, 0.2) for real sequences. Our method is run in

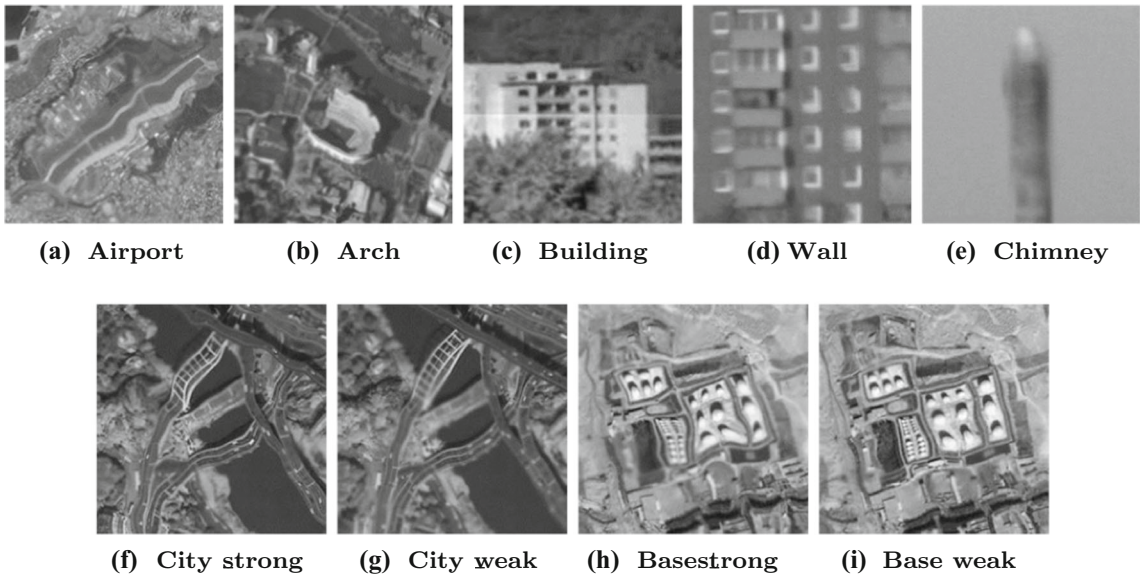

Fig. 3 Gallery of test videos. We refer to the videos by its name in our experiments

Matlab7.11.0 with MEX on a Dell Optiplex 990 with Intel CPU 3.4GHz and 8 GB memory.

Our method is compared with six state-of-the-art methods: near-diffraction-limited-based image reconstruction for removing turbulence [6] (NDL), deformation-guided kernel regression (DGKR) [22], Bregman iteration and nonlocal total variance for atmospheric turbulence stabilization [12] (BNLTV), the data-driven two-stage approach for image restoration [35] (Two-stage), principal components analysis for atmospheric turbulence [9] (PCA), and the lucky region method [21] (Lucky region). The literature [35] aimed at restoring an image from a sequence distorted by water waves. Its application scenario is different from ours, but the method [35] achieved reasonable results when it comes to handle the air turbulence. Therefore, it is reasonable to compare this method with our approach. We use the source codes of Twostage [35], NDL [6], and DGKR [22] provided by their respective authors and we use the default settings for the parameters.

5.2 Simulated experiments

We compare the performances of seven image restoration methods in terms of peak signal-to-noise ratio (PSNR) and structural similarity (SSIM). We show the comparison results in Table 3. Each method has two data for each video, PSNR is shown in the top, and SSIM is shown in the bottom. The size of the video frame is given in the bracket of the leftmost column. From Table 3, it demonstrates that the proposed method achieves not only the best PSNR results but also the best SSIM results in all the seven simulated degraded videos with a considerable performance gap from other approaches. Especially, our method achieves the average gain of 1.27 and 0.15 in PSNR and SSIM compared with the recent proposed NDL [6]. Compared with our previous work DGKR [22], the proposed method achieves the average gain of 1.08 and 0.05 in PSNR and SSIM.

The visual effect comparisons are given in Figs. 4, 5. In Fig. 4, the enlarged areas indicate that our method can produce much sharper edges than others and generate the best visual effect. In Fig. 5, we show the subjective assessments for the rest simulated videos. The result generated by lucky region method does not look better than the

Table 1 The parameter settings used in simulated videos

	Interval of control points d_g	Variance of the Gaussian distribute of control points δ_d^2	Variance of Gaussian noise δ_n^2
Weak turbulence	32	4	3
Strong turbulence	16	10	16

Table 2 Parameter settings in our experiments

ε_x, ε_y	16	The intervals of the control points in the registration
L	13	The patch size in the registration
L_{nl}	5×5	The local patch size in the nonlocal total variation
W	21×21	The search window size in the nonlocal total variation
N	10	The number of best neighbors in nonlocal total variation
λ	1.5	The parameter in Eq. (15)
μ_1	0.25	The balance parameter for the SKRTV term in Eq. (14)
μ_2	0.25	The balance parameter for the NLTV term in Eq. (14)
W_{wnnm}	5×5	The image patch size used in video denoising
h_k	1	The kernel width used in SKRTV of Eq. (7)
h_n	20	The kernel width used in NLTV of Eq. (6)

Table 3 The comparison results of the six image restoration methods in terms of PSNR and SSIM

Example	Lucky region	PCA	Twos- tage	BNLTV	NDL	DGKR	Ours
Airport_distort	22.1312	18.6877	23.5086	23.8537	22.5819	23.8137	24.0577
(260×260)	0.4453	0.3432	0.6063	0.6247	0.4933	0.7207	0.7803
Arch_distort	23.3630	17.2758	23.1663	23.9025	25.2866	25.160	26.1818
(260×260)	0.6649	0.5301	0.6580	0.7057	0.7723	0.8014	0.8311
City_strong	20.3783	15.8282	21.9903	22.8921	21.2538	21.9172	22.9349
(260×260)	0.4500	0.3121	0.6448	0.6854	0.5300	0.7063	0.7486
City_weak	21.9876	18.1330	21.8451	23.0246	23.8894	24.117	25.2938
(260×260)	0.6045	0.4573	0.6230	0.6932	0.7257	0.7642	0.8271
Base_strong	20.1338	11.8681	22.3870	22.3401	22.0113	22.4812	23.8403
(256×256)	0.4668	0.2461	0.6797	0.6679	0.6082	0.7731	0.8141
Base_weak	21.7177	12.1593	23.211	25.3293	25.0282	23.6918	25.3536
(256×256)	0.6027	0.3075	0.7532	0.8387	0.7952	0.8492	0.8827

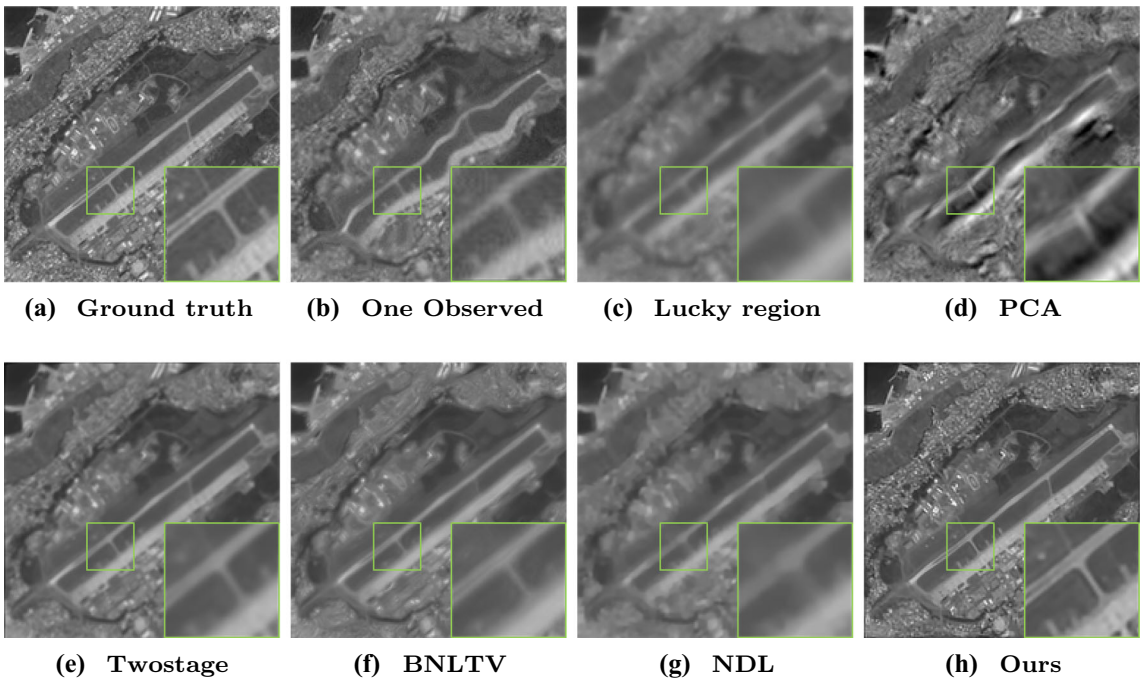

Fig. 4 Image restoration results on the simulated Airport video, with the region in the bounding boxed enlarged for better visualization

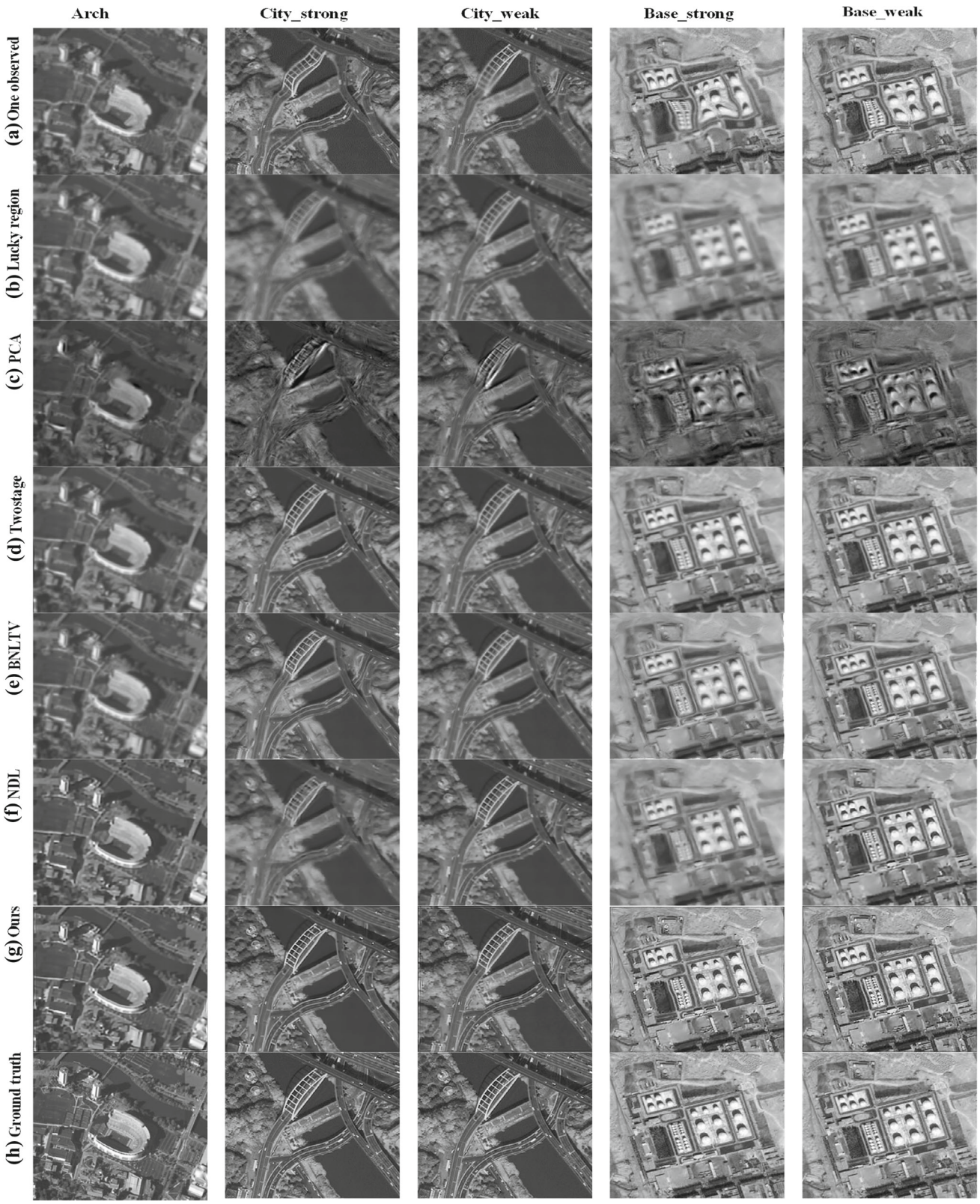

Fig. 5 Comparison of visual effects for the simulated videos

result generated by the temporal average. The results of the PCA-based method looks unnatural. The BNLTV achieves better visual effect than either the lucky region method or the PCA-based method, but some detail structures are not

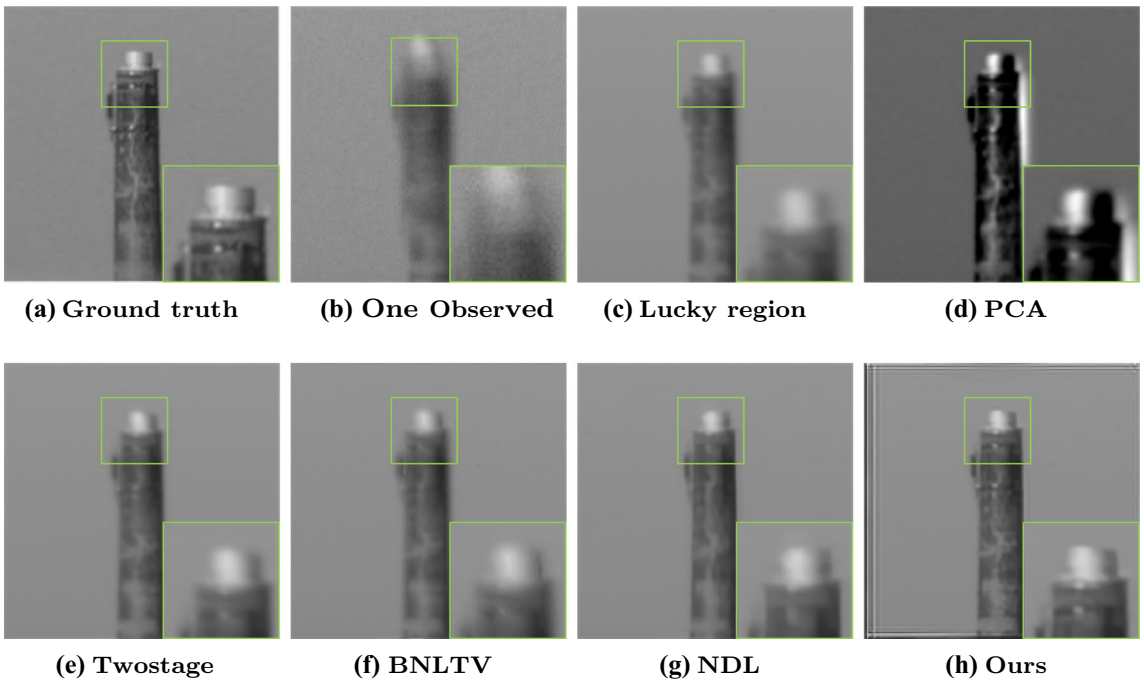

Fig. 6 Image restoration results on the real Chimney video

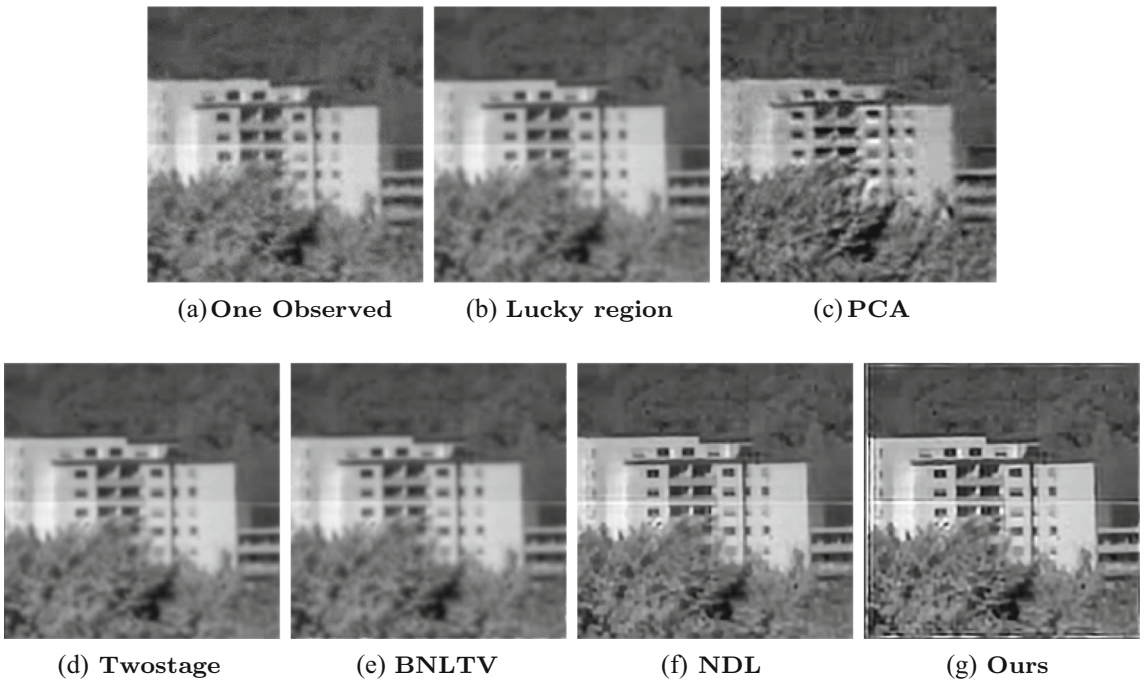

Fig. 7 Image restoration results on the real Building video

restored. The BNLTV uses the nonlocal similarity to constrain the image restoration model, so the result looks smoother. The results generated by the two-stage and NDL methods are similar, where most of the high-frequency distortion can be recovered. However, minor blur effects are still observed. The proposed method can improve the visual greatly and recover the high-frequency detail well. The proposed method is better than the other comparative methods just because we improve not only the quality of the reference image but also the quality of near-diffraction-limited image.

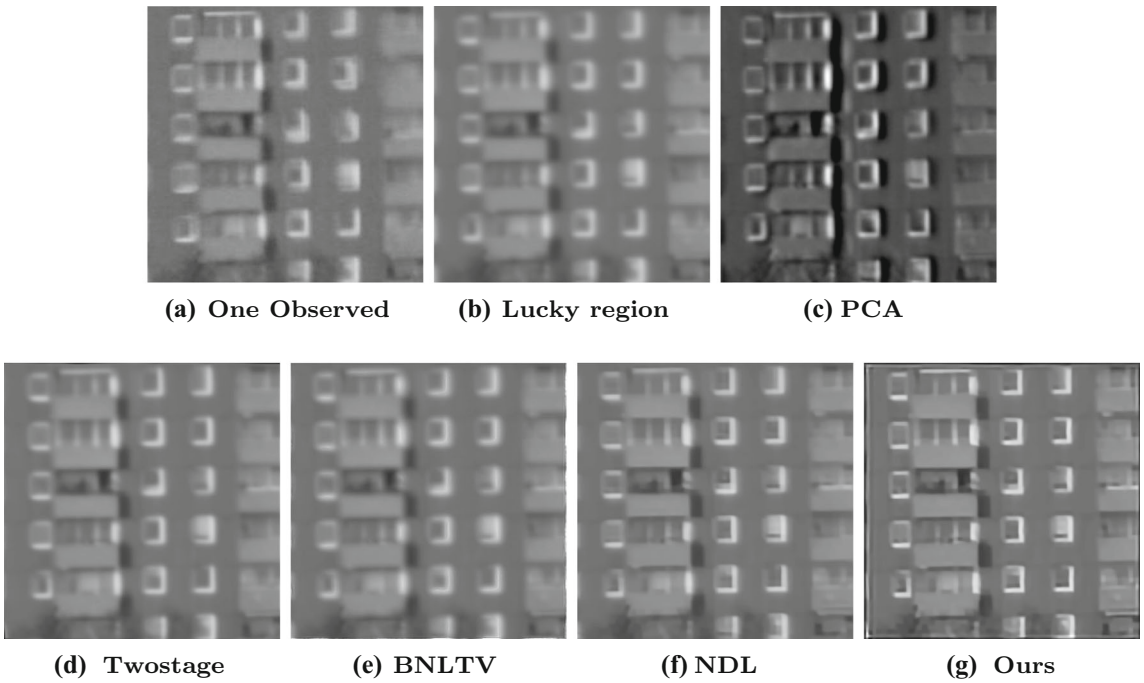

Fig. 8 Image restoration results on the real Wall video

5.3 Real video experiments

Experiments are conducted on videos from real scenario. Since most of them do not have the ground truth images, only qualitative results are presented. Figures 6, 7, and 8 show the final outputs of all methods. In Fig. 6, the enlarged areas indicate that our method can produce sharper edge than the others and achieves the best visual effect. In the six comparative methods, only our method and NDL can remove the diffraction-limited blur and produce sharp restored images, while the other methods cannot remove the diffraction-limited blur. However, the results of NDL contain halo artifact near the edges, which can be seen clearly in the edges of the building and the windows. The halo artifact is produced due to both the noises introduced by the sensor and registration error and the inaccurate PSF estimation. Both our method and NDL use the same deconvolution algorithm using the same parameters to generate the output, so we infer that noises are the main factor to result in artifacts and our denoising algorithm based on WNNM is able to effectively reduce the video noises.

5.4 Effect of the intermediate operations

Firstly, we show that the reference image enhancement is able to improve image registration. In Fig. 9, we present two example results to compare the reference image initialization methods. The first column contains three observed frames, the second column is the results of temporal averages, and the third column is the results of low rank decomposition. As we observed, the temporal averages look more blurring than the reference images generated by low-rank decomposition, which is obvious for the stronger turbulence frames. The difference between the results of temporal average and low-rank decomposition is clear in both *Airport* and *City_strong*, while it is not obvious in *Chimney*. The low-rank decomposition method is able to generate sharper edges than the temporal average method and the former is better than the latter in visual effect.

Furthermore, we also discuss how the regularization term influences the performance of turbulence removal. Regarding the effect of the regularization term, we design two methods: (1) SKRTV* only uses the SKRTV regularization term and other configurations are fixed, (2) NLTV* only uses the NLTV regularization terms and other configurations are fixed. The comparison results are shown in Table 4. The results show that the joint regularization method is superior to any of the single regularization method. The average gains of PSNR and SSIM are (0.54, 0.015) and (0.43, 0.019) for only NLTV and only SKRTV, respectively. It further shows the effectiveness of the joint regularization model.

Finally, we show the effects of the intermediate operations: reference image initialization based on RPCA, image registration based on the joint regularization model, near-

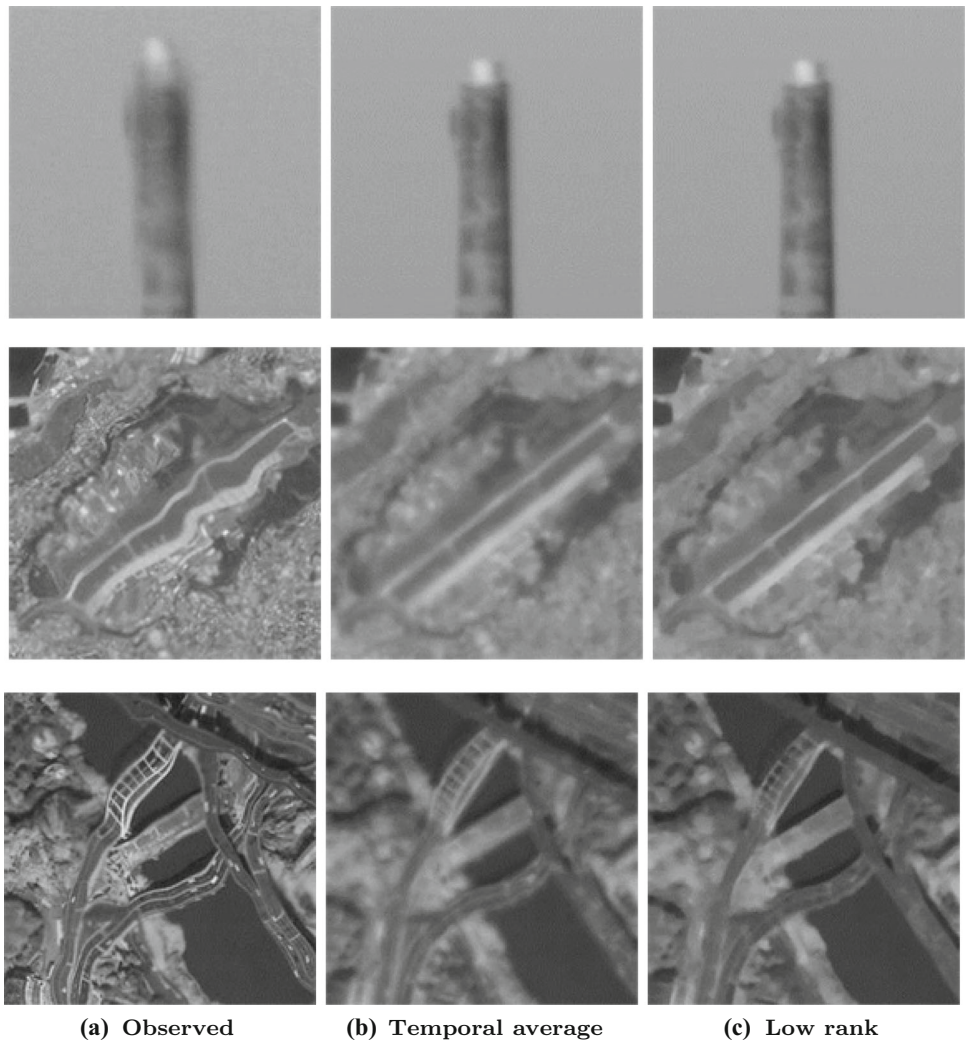

Fig. 9 Comparison of the reference images generated by the temporal average method and the RPCA method. **a** One observed frame. **b** The reference images generated by the temporal average method. **c** The reference image generated by the RPCA method

Table 4 The comparison of the regularization methods on six simulated videos

	SKRTV*	NLTV*	Ours
Airport_distort	23.6625	23.6584	24.0577
(260×260)	0.7496	0.7544	0.7803
Arch_distort	25.8455	25.9478	26.1818
(260×260)	0.8126	0.8127	0.8311
City_strong	22.6639	22.6164	22.9349
(260×260)	0.7451	0.7445	0.7486
City_weak	24.8078	25.2764	25.2938
(260×260)	0.7920	0.8078	0.8271
Base_strong	23.3852	23.3414	23.8403
(256×256)	0.8086	0.8054	0.8141
Base_weak	24.0368	24.2157	25.3536
(256×256)	0.8644	0.8687	0.8827

diffraction-limited image reconstruction based on WNNM, deconvolution. For example, Fig. 10 shows the intermediate results of *City_strong*. It shows that the low-rank part is lack of inner structure. The iterative image registration based on joint regularization makes the reference image clearer than the initial reference image in visual effect. The WNNM algorithm makes the image clearer and sharper and can restore most detailed structures. After deconvolution, the image in Fig. 10d is the most sharpest and clearest. Moreover, the numerical results of PSNR and SSIM also show that the joint regularization model can make the quality of the observed frame better step by step. WNNM can boost the restoration performance than joint regularization, and deconvolution achieves the best performance. We also present the intermediate results of all the experimental videos in Table 5. It is observed that the PSNRs of the initialization method based on the temporal average are almost greater than those based on the low-rank fusion except the videos of *Arch* and *Base_strong*. But the SSIMs of the low-rank fusion method are all higher than the

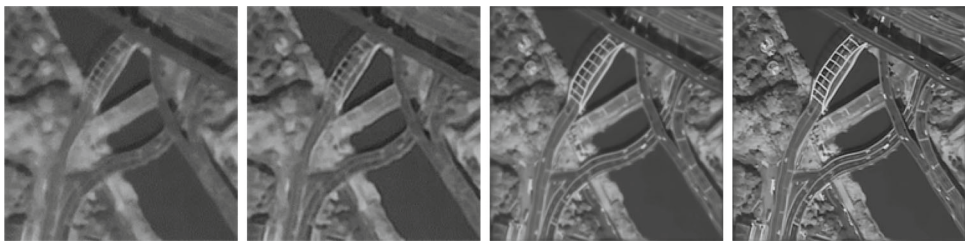

(a) Low-rank (20.1427/0.4854) **(b) SKRTV+NLTV** (20.5961/0.5355) **(c) WNNM** (22.7306/0.6882) **(d) Deblurring** (22.9349/0.7486)

Fig. 10 The middle result comparison on the *City_strong* video. **a** The reference image generated by RPCA. **b** The result of geometric correction via SKRTV and NLTV. **c** The result of video denoising via WNNM. **d** The deblurring result

Table 5 The comparison of the initialization method and the intermediate operations

	Mean	Low rank	NL_SKR_TV	WNNM	Final results
Airport_distort	22.1001	21.9587	22.353	23.7941	24.0577
(260×260)	0.4395	0.4754	0.5214	0.6552	0.7803
Arch_distort	23.2848	23.4284	24.7101	24.0756	26.1818
(260×260)	0.6544	0.6810	0.7572	0.7129	0.8311
City_strong	20.3620	20.1427	20.5961	22.7306	22.9349
(260×260)	0.4467	0.4854	0.5355	0.6882	0.7486
City_weak	21.8512	21.8497	22.784	23.0232	25.2938
(260×260)	0.5873	0.6028	0.6741	0.6887	0.8271
Base_strong	20.1179	20.6704	21.5198	23.0322	23.8403
(256×256)	0.4629	0.5317	0.6037	0.7229	0.8141
Base_weak	21.6569	22.3770	23.3399	24.7610	25.3536
(256×256)	0.5925	0.6674	0.7368	0.8230	0.8827

initialization method based on the temporal average. Combining the visual effect, the low-rank fusion method is superior to the averaging method. It is also observed that each intermediate operation boosts the performance progressively on almost all video sequences except the *Arch*. Thus, it demonstrates that our method is effective for turbulence removal.

5.5 Analysis of time complexity

The computational complexity of the proposed work is high which is similar to the reference [6]. In the first stage of low-rank matrix decomposition, the computational complexity is about $O(n^3)$, in the geometric correction, the complexity is about $O(K^2 * L^2 * n^3 * t)$ where K and L are the number of the outer and inner grids and t is the number of frames, and in the last stage, the computational complexity is $O(n^3)$. It spends about one minute to process a frame.

6 Conclusions and future work

In this paper, we aim to remove the atmospheric turbulence of the degraded videos based on the effective image prior knowledge such as nonlocal similarity, local smoothness, and low-rank property. The turbulence removal has two challenging sub-tasks: spatially and temporally variant blur reduction and the geometric distortion reduction. Thus, we propose a systematic method which jointly uses regularization and low-rank fusion to solve the turbulence removal. Concretely, in order to correct the local distortion, low-rank decomposition is used to generate a better reference image. Then, to further improve the registration, we propose the joint TV regularization with SKRTV and NLTV for the optimization problem. SKRTV is used for preserving the local structures of the image and NLTV is used for remaining the similarity of the nonlocal repetitive structures or textures. In order to solve the TV-based optimization problem, we develop a novel algorithm based on SBI. Furthermore, to alleviate blur variation, we implement WNNM on the registered frames, which results in a near-diffraction-limited image. At last, we adopt a space-invariant blind deconvolution method to make the diffraction-limit image deblur. We do extensive

experiments for evaluation of our method on the simulated and real videos, and the experimental results demonstrate that our method is superior to the state-of-the-art methods and the gain of PSNR and SSIM is remarkable. In the future, we will try to use the deep learning method to solve the turbulence removal and study the method with real-time processing.

Acknowledgements This work is supported by the National Key Research and Development Program of China No. 2020AAA0108301, the National Natural Science Foundation of China under Grant Nos. 61876161 and 61772524, the Natural Science Foundation of Shanghai (20ZR1417700), the CAAI-Huawei MindSpore Open Fund and the Fundamental Research Funds for the Central Universities.

Declarations

Conflict of interest The authors declare that they have no conflict of interest.

References

1. Han M, Lyu Z, Qiu T, Xu M (2018) A review on intelligence dehazing and color restoration for underwater images. IEEE Trans Man Cybern Part A Syst Hum 50:1820–1832
2. Yuan Q, Zhang L, Shen H (2014) Hyperspectral image denoising with a spatial spectral view fusion strategy. IEEE Trans Geosci Remote Sens 52(5):2314–2325
3. Li W, Zhang D, Liu Z, Qiao X (2005) Fast block-based image restoration employing the improved best neighborhood matching approach. IEEE Trans Syst Man Cybern Part A Syst Hum 35(4):546–555
4. Hong J, Cho S, Cho U (2009) A novel evolutionary approach to image enhancement filter design: method and applications. IEEE Trans Syst Man Cybern Part B Cybern 32(11):1446–1457
5. Bue BD, Thompson DR, Eastwood M, Green RO (2015) Real-time atmoshperic correction of AVIRIS-NG imagery. IEEE Trans Geosci Remote Sens 53(12):6419–6428
6. Zhu X, Milanfar P (2013) Removing atmospheric turbulence via space-invariant deconvolution. IEEE Trans Pattern Anal Mach Intell 35:157–170
7. Molina R, Nunez J, Cortijo FJ, Mateos J (2001) Image restoration in astronomy: a Bayesian perspective. IEEE Signal Process Mag 18:11–29
8. Pantin E, Starck J-L, Murtagh F (2007) Deconvolution and blind deconvolution in astronomy. In: Blind image deconvolution: theory and applications, pp 100–138
9. Li D, Mersereau RM, Simske S (2007) Atmospheric turbulence-degraded image restoration using principal components analysis. IEEE Geosci Remote Sens Lett 4:340–344
10. Harmeling S, Hirsch M, Sra S, Scholkopf B (2009) Online blind deconvolution for astronomical imaging. In: IEEE international conference on in computational photography, pp 1–7
11. Tahtali M, Lambert A, Fraser D (2008) Self-tuning Kalman filter estimation of atmospheric warp. In: Proceedings of SPIE, vol 70760F
12. Mao Y, Gilles J (2012) Non rigid geometric distortions correction-application to atmospheric turbulence stabilization. Inverse Probl Imaging 6:531–546
13. Shimizu M, Yoshimura S, Tanaka M, Okutomi M (2008) Super-resolution from image sequence under influence of hot-air optical turbulence. In: IEEE conference on computer vision and pattern recognition, pp 1–8 (2008)
14. Zhu X, Milanfar P (2010) Image reconstruction from videos distorted by atmospheric turbulence. In: Proceedngs of SPIE, vol 7543
15. Hirsch M, Sra S, Scholkopf B, Harmeling S (2010) Efficient filter flow for space-variant multiframe blind deconvolution. In: CVPR
16. Roggemann MC, Stoudt CA, Welsh BM (1994) Image-spectrum signal-to-noise-ratio improvements by statistical frame selection for adaptive-optics imaging through atmospheric turbulence. Opt Eng 33:3254–3264
17. Vorontsov MA, Carhart GW (2001) Anisoplanatic imaging through turbulent media: image recovery by local information fusion from a set of short-exposure images. J Opt Soc Am 18(6):1312–1324
18. Tubbs RN (2003) Lucky exposures: diffraction limited astronomical imaging through the atmosphere. arXiv:astro-ph/0311481
19. Fried DL (1978) Probability of getting a lucky short-exposure image through turbulence. J Opt Soc Am 68:1651–1657
20. Joshi N, Cohen M, Rainier SM (2010) Lucky imaging for multi-image denoising, sharpening, and haze removal. In: IEEE international conference of computational photography
21. Aubailly M, Vorontsov MA, Carhart GW, Valley MT (2009) Automated video enhancement from a stream of atmospherically-distorted images: the lucky-region fusion approach. In: Proceedings of SPIE—the international society for optical engineering, vol 7463
22. Xie Y, Zhang W, Tao D, Hu W, Qu Y, Wang H (2016) Removing turbulence effect via hybrid total variation and deformation-guided kernel regression. IEEE Trans Image Process 25(10):4943–4958
23. Gu S, Zhang L, Zuo W, Feng X (2014) Weighted nuclear norm minimization with application to image denoising. In: IEEE conference on computer vision and pattern recognition, pp 2862–2869
24. Cands EJ, Li X, Ma Y, Wright J (2011) Robust principal component analysis? J ACM 58:11
25. Wang S, Zhang L, Liang Y (2012) Nonlocal spectral prior model for low-level vision. ACCV 2012:231–244
26. Mao Y, Gilles J (2012) Non rigid geometric distortions correction-application to atmospheric turbulence stabilization. Inverse Probl Imaging 6(3):531–546
27. Myronenko A, Song X (2010) Intensity-based image registration by minimizing residual complexity. IEEE Trans Med Imaging 29(11):1882–1891
28. Takeda H, Farsiu S, Milanfar P (2007) Kernel regression for image processing and reconstruction. IEEE Trans Image Process 16:349–366
29. Goldstein T, Osher S (2009) The split Bregman method for L1-regularized problems. SIAM J Imaging Sci 2:323–343
30. Gilboa G, Osher S (2008) Nonlocal operators with applications to image processing. Multisc Model Simul 7:1005–1028
31. Xie Y, Qu Y, Tao D, Wu W, Qu Y, Zhang W (2016) Hyperspectral image restoration via sparse and low-rank matrix recovery. IEEE Trans Geosci Remote Sens 54(8):4642–4659
32. Shan Q, Jia J, Agarwala A (2008) High-quality motion deblurring from a single image. In: ACM transactions on graphics, p 73
33. Nagy JG, Oleary DP (1997) Fast iterative image restoration with a spatially varying PSF. In: International society for optics and photonicsin, advanced signal processing: algorithms, architectures, and implementations VII, vol 3162, pp 388–399
34. Stockham Jr TG (1966) High-speed convolution and correlation. In: Proceedings of spring joint computer conference, pp 229–233

35. Oreifej O, Shu G, Pace T, Shah M (2011) A two-stage reconstruction approach for seeing through water. In: IEEE conference on in computer vision and pattern recognition, pp 1153–1160